RSC Advances

PAPER

View Article Online
View Journal | View Issue

Cite this: *RSC Adv.*, 2016, **6**, 90401

Cooperative assembly synthesis of mesoporous $SrTiO_3$ with enhanced photocatalytic properties†

Buğra E. Kayaalp,[a] Young Joo Lee,[a] Andreas Kornowski,[b] Silvia Gross,[cd] Massimiliano D'Arienzo[e] and Simone Mascotto*[a]

Received 27th May 2016
Accepted 10th September 2016

DOI: 10.1039/c6ra13800d

www.rsc.org/advances

The synthesis of mesoporous $SrTiO_3$ by using the cooperative assembly of metal chelate complexes and alkoxysilanes is here presented. The high affinity and intimate mixing between the two precursors fostered the formation, *via* polycondensation, of interpentrating organic and inorganic polymers. Hence, after calcination and removal of the siliceous phase, aggregates of mesoporous, polycrystalline $SrTiO_3$ with interconnected pores of *ca.* 10 nm and surface areas as high as 240 $m^2\ g^{-1}$ were obtained. Systems using different $SrTiO_3$: SiO_2 molar ratios were prepared to vary the porosity and microstructure. The templating action of the silica and its effect on the physicochemical properties of the final porous materials were addressed by a multi-technique approach. Finally, the activity of the bulk mesoporous $SrTiO_3$ systems was exemplarily demonstrated by photodegradation tests of methylene blue under UV light. The dye conversion progressively increased with the content of silica template, proving the higher activity of the proposed mesoporous materials.

Introduction

Strontium titanate ($SrTiO_3$) can be considered as a model perovskite system, thanks to the ease in accommodating non-stoichiometry and to its polarizability. The ferroelectric properties,[1] relatively high band gap (3.25 eV, $\lambda = 361$ nm)[2] and mixed ionic-electronic conductivity[3,4] make this material very interesting for a wide range of applications, such as thermoelectrics,[5,6] memristive devices,[7] capacitors,[8] photocatalysis[9] and anode materials in solid oxide fuel cells.[10]

In order to profit from this wide application potential, the improvement of the textural properties is crucial. With respect to this, a central issue is the achievement of a high specific surface area and pore volume.

Recently, diverse works showed the preparation of mesoporous $SrTiO_3$ nanoparticles for photocatalytic applications.[11–16] Ouyang & Ye[12] presented the synthesis of mesoporous $SrTiO_3$ nanoparticles by hydrothermal method using silica spheres (10–20 nm) as nanotemplate. The materials showed interesting activity in photodegradation of 2-propanol to acetone. A molten salts route was employed by Liu *et al.*[13] for the synthesis of porous $SrTiO_3$ nanocrystals with improved photocatalytic hydrogen evolution. Hydroxide salt melts acted both as solvent and template generating porous crystalline nanostructures by aggregative growth mechanism.

The synthesis protocols for mesoporous $SrTiO_3$ nanoparticles are usually based on low temperature ($T < 250$ °C) solvothermal processes. Hence, potential structural and morphological modifications of the porous texture limit their employment to room temperature applications, *e.g.* photocatalysis. The preparation of mesoporous bulk $SrTiO_3$ would be therefore desirable to widen the application range, exploiting the larger particle size and higher thermal stability. However, with respect to the nanoparticulate systems, the synthesis of bulk materials is much more challenging and therefore less represented in the literature.

Among the diverse wet synthesis approaches (*e.g.* sol–gel, co-precipitation), perovskite oxide materials can be prepared using molar excess of chelating agent such as citric acid, ethylene glycol or oxalate to ensure homogeneous mixing of the cations at the molecular scale and avoid secondary phase formation.[17–19]

In this respect, synthesis strategies commonly used for porous oxide structures such as evaporation induced self-assembly (EISA)[20] may not be the best choice to prepare $SrTiO_3$ with large surface area. Firstly, metal chelate complexes are poor nanobuilding blocks for self-assembly.[21] Secondly, soft templates used in EISA process usually decompose at

[a]*Institut für Anorganische und Angewandte Chemie, Universität Hamburg, Martin-Luther-King Platz 6, D-20146 Hamburg, Germany. E-mail: simone.mascotto@chemie.uni-hamburg.de*

[b]*Institut für Physikalische Chemie, Universität Hamburg, Grindelallee 117, D-20146 Hamburg, Germany*

[c]*Dipartimento di Scienze Chimiche, Università Degli Studi di Padova, via Marzolo, 1, I-35131, Padova, Italy*

[d]*Istituto per l'Energetica e le Interfasi, IENI-CNR and INSTM, UdR Padova, via Marzolo, 1, I-35131, Padova, Italy*

[e]*Dipartimento di Scienza Dei Materiali, INSTM, Università di Milano-Bicocca, via R. Cozzi, 55, I-20125, Milano, Italy*

† Electronic supplementary information (ESI) available. See DOI: 10.1039/c6ra13800d

temperatures below the crystallization of perovskite, causing collapse of the mesostructure. Hence, only few works report the preparation of nanoporous bulk $SrTiO_3$ systems *via* soft templating.[22,23]

In the past years, the co-assembly, *i.e.* cooperative assembly, process of alkoxysilane and resol was successfully adopted to prepare carbon/silica nanocomposites.[24,25] The main point of this approach is the intimate molecular intermixing of the inorganic and organic precursors given by their high concentration of hydroxyl groups. These functionalities promote sol–gel reactions to form highly homogeneous interpenetrating networks. After removal of one of the polymers, either highly porous carbon or silica can be obtained.

Herein, we show how the co-assembly principle can be used as an easy and reproducible approach towards the synthesis of bulk mesoporous polycrystalline $SrTiO_3$ with large porosity. Chelating agents such as citric acid and glycerol represent here the carbon precursors and are further used to complex the metal ions. Pre-hydrolyzed alkoxysilane is added as silica source and porogen. Subsequently, the reaction temperature is increased to promote polycondensation, *i.e.* co-assembly, of the carboxy and silanol groups until gelation occurs. After removal of the carbonaceous component by high temperature treatment, interpenetrating $SrTiO_3/SiO_2$ nanocomposites are obtained. The presence of the hard siliceous endotemplate allows the formation and the stabilization of the crystalline $SrTiO_3$ network at high temperatures preventing the mesostructured from shrinking. Hence, further etching of silica network by NaOH leads to highly porous perovskite with well interconnected pores and pore volume and surfaces area as high as 0.39 $cm^3\ g^{-1}$ and 240 $m^2\ g^{-1}$, respectively. The composition ratio $SiO_2/SrTiO_3$ was tuned between 0.1 and 1 to modulate the textural properties such as porosity and crystallinity of the final system. The physicochemical properties of the materials were investigated by a multi-technique approach in order to determine the structure–function relationships. The activity of the proposed porous bulk $SrTiO_3$ was studied in regard to photochemical dye degradation under UV-light and compared with the conventional nanoparticulate systems.

Experimental

Chemicals and materials

Strontium nitrate (99%, Acros Organics), titanium(IV) isopropoxide (98%, ABCR), TEOS (98%, Alfa Aesar), citric acid (99%, ABCR), glycerol (99%, Alfa Aesar), sodium hydroxide (98.5%, Acros Organics), hydrochloric acid (37%, VWR), ethanol (99.8%, VWR) and glacial acetic acid (HOAc 99%, VWR) were used as received without further purifications. Nanoparticulate $SrTiO_3$ (np_$SrTiO_3$) was purchased from chemPUR.

Synthesis of the pre-hydrolyzed TEOS solution

61 ml of TEOS were mixed with 61 ml of ethanol. Subsequently 6.9 ml of HCl (0.02 M) were added dropwise. The mixture was stirred for 90 min at 60 °C and then stored at 4 °C.[26]

Synthesis of the mesoporous $SrTiO_3$

Mesoporous $SrTiO_3$ was prepared *via* the chelate complex method using the co-assembly approach. In a typical synthesis 5.43 mmol of titanium(IV) isopropoxide were added to 11.9 ml of glycerol by stirring at room temperature for 30 min. Glycerol was preferred over the standardly used ethylene glycol owing to its better chelating and crosslinking properties. Subsequently, 40.7 mmol of citric acid were added and the temperature was raised up to 60 °C. 5.43 mmol of $Sr(NO_3)_2$ were added to the mixture at this temperature and, after complete dissolution, the silica source was finally introduced in stoichiometric ratios $SiO_2/SrTiO_3$ from 0.1 to 1. After equilibration for 2 hours, the temperature was raised up to 130 °C under vigorous stirring to promote the polycondensation reactions between the chelating agents. The resulting polymer gel was calcined at 600 °C for 2 h in air to eliminate the organic component. The temperature was increased at a rate of 2 °C min^{-1} and held at 350 °C for 2 h before reaching the final temperature. The $SiO_2/SrTiO_3$ nanocomposites (Scheme 1) were treated with 2 M NaOH solution at 90 °C to remove the silica phase. After neutralization to pH = 7 with water, the materials were washed with 1.75 mM glacial acetic acid at room temperature to eliminate $SrCO_3$ impurities.[27] Both treatments were carried out one time using 50 ml of solution for each 350 mg of material, under stirring in a closed vessel for 24 h. The prepared materials were named after the $SrTiO_3$: SiO_2 molar ratios. The sample labeled as "no template" represents $SrTiO_3$ obtained without SiO_2 template.

X-ray diffraction

X-ray diffraction analysis was carried out with an X'Pert Pro diffractometer (PANalytical Corp.) with 1.5406 Å Ni-filtered Cu-Kα radiation, operating at 45 kV and 40 mA, step size 0.0130°, step time 74 s per step. The mean crystallite sizes were

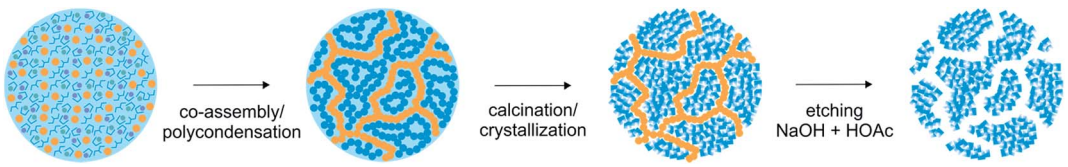

Scheme 1 Formation mechanism of the nanoporous $SrTiO_3$. The yellow and blue symbols represent the silica and the complex-polymer/$SrTiO_3$ respectively. At the beginning all the molecular precursors are homogeneously distributed in the reaction environment. Once the polycondensation takes place silica and polyester networks grow intimately. The NaOH and HOAc treatment of the $SiO_2/SrTiO_3$ nanocomposites obtained after calcination leads to nanoporous $SrTiO_3$ with interconnected pores.

calculated from the full width at half maximum (FWHM) of the most intense reflection using the Scherrer equation.

Nitrogen physisorption

The nitrogen sorption isotherms were obtained at 77 K using a Quadrasorb SI-MP by Quantachrome. Outgassing was performed with a Masterprep Degasser (Quantachrome Corp.) at 120 °C for 10 h. Specific surface areas were determined with the Brunauer–Emmett–Teller (BET) method[28] at $p/p_0 = 0.07–0.3$. Pore size distribution was determined with the NLDFT method[29] applying the model for cylindrical pores on the adsorption branch by using the Quantachrome ASiQWin software.

^{29}Si NMR spectroscopy

^{29}Si cross polarization magic angle spinning nuclear magnetic resonance (CPMAS NMR) experiments were performed at an operating frequency of 79.52 MHz on a Bruker AvanceII 400 spectrometer equipped with a 4 mm double resonance probe. ^{1}H 90°pulse length of 4.4 μs, contact time of 2 ms, and recycle delay of 5 s were used. All the measurements were performed at room temperature and with the MAS frequency of 5 kHz. Continuous wave decoupling was used during the acquisition. 16 000 transients were acquired for all the samples and the spectra were plotted in a calibrated intensity scale, taking into account the analyzed sample mass.

Infrared spectroscopy

Infrared (IR) spectra were obtained on KBr pellets in the region 400–4000 cm^{-1} in transmission mode with a Bruker Vertex 70 FTIR spectrophotometer.

Thermogravimetric analysis

Thermal characterization was carried out using a NETZSCH STA 449F3 coupled with Äeolos QMS403C (TG – MS) with 10 °C min^{-1} heating rate in an Ar/O_2 stream (volume ratio 78/22).

Electron microscopy

Scanning electron microscopy (SEM) images were obtained on a LEO1550 with a spatial resolution of ≈1 nm. The powder was fixed on a standard carbon conductive tab and was investigated without further conductive coating.

Transmission electron microscopy (TEM) measurements were carried out on a JEOL JEM 2200 FS at 200 kV equipped with two CEOS Cs correctors (CETCOR, CESCOR), a Gatan 4K UltraScan 1000 camera and a HAADF (high angle annular dark field) detector. The sample was crushed into a fine powder, which was suspended in toluene by sonication and dropped on a carbon coated 400 mesh TEM grid. The excess of solvent was removed with a filter paper and by drying the grid under air.

X-rays photoelectron spectroscopy (XPS)

XPS spectra were acquired by using a Perkin-Elmer Φ 5600ci spectrometer using standard Al radiation (1486.6 eV) working at 250 W. The working pressure in the analysis chamber was <5 10^{-8} Pa. The spectrometer was calibrated by assuming the binding energy (BE) of the Au $4f_{7/2}$ line at 83.9 eV with respect to the Fermi level. The standard deviation for the BE values was 0.15 eV. The reported BE were corrected for the charging effects, assigning to the C 1s line of adventitious carbon the BE value of 284.6 eV.[30,31]

Survey scans (187.85 pass energy, 1 eV per step, 25 ms per step) were obtained in the 0–1350 eV range. Detailed scans (29.35 eV pass energy, 0.1 eV per step, 100–150 ms per step) were recorded for the C 1s, O 1s, Ti 2p, Sr 3d, Si 2p, TiLMM regions. The atomic composition of the powders, after a Shirley type background subtraction[32] was evaluated using sensitivity factors supplied by Perkin-Elmer.[31] The assignments of the peaks was carried out by using the values reported in the reference handbook.[31]

Photocatalytic dye degradation

Dye degradation tests were performed with a 125 W high pressure mercury vapor UV lamp (Philips HPK-125W, maximum radiation at $\lambda = 365$ nm, full spectrum Fig. S1†) encased in constant coolant water circulation apparatus. Accordingly to ref. 11 and 33 50 ml of water-based methylene blue solution (50 mg l^{-1}) was treated with 50 mg $SrTiO_3$ photocatalyst powder in a 100 ml glass beaker placed 10 cm directly under the light source (irradiance at surface *ca.* 30 Wm^{-2} nm^{-1}, see ESI†). Saturation of dye adsorption was reached after 1 h of dark stirring (Fig. S2a†). Methylene blue samples were investigated *via* UV-Vis spectroscopy after 0 min, 20 min, 60 min and 120 min of irradiation. Additional experiments were performed without catalyst to exclude spontaneous dye degradation under UV light (Fig. S2b†). Each sample (1 ml) was diluted with H_2O to 10 ml and centrifuged at 10 000 rpm for 30 min to eliminate possibly suspended $SrTiO_3$ particles. The UV/Vis spectra of the methylene blue solutions and of the porous $SrTiO_3$ samples were recorded with a Cary 5000 UV/Vis-NIR spectrophotometer of Varian. The powder measurements were performed using a Praying Mantis Diffuse Reflection Accessory by Harrick, dispersing 50 mg of material in 150 mg of $BaSO_4$ standard. Obtained reflectance spectra were converted to the Kubelka Munk function $F(R)$ with Cary WinUV software.

Results and discussion

Thermogravimetric analysis was at first performed to verify the thermal stability of the nanocomposite systems. Thermograms (Fig. 1) show mass loss for all the samples up to *ca.* 550 °C. Based on these results, 600 °C was chosen as final temperature for the calcination of the materials. The microstructure was investigated using powder X-ray diffraction. The nanocomposites, especially those with high silica amount, present mixed phases ascribed to $SrTiO_3$, $SrCO_3$ and SiO_2-based compounds (Fig. 2a–c). Conversely, after etching, pure $SrTiO_3$ phase was detected. The average crystallite size (Φ, Table 1) decreases upon increasing SiO_2 content as a result of the diffusion barrier on the mass transport.

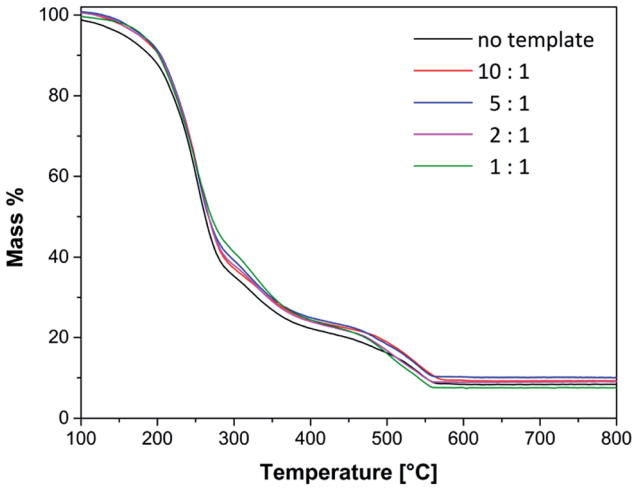

Fig. 1 Thermograms of the polymer-gels with different $SrTiO_3$: SiO_2 molar ratios.

In order to deeply investigate the complete etching of silica and carbonates, and have a clear picture of the materials composition, spectroscopic methods (IR, ^{29}Si NMR, XPS) were employed. Infrared spectroscopy could clearly determine the effective removal of carbonates ($\nu = 1460\ cm^{-1}$) after the acetic acid etching procedure (Fig. 2d). The same trend can be observed for silica after NaOH etching. However, in this case no precise conclusions can be drawn from the IR spectra due to the broad and blunt signal at *ca.* $\nu = 1000\ cm^{-1}$.

Better understanding of the silica structure and its removal could be obtained by ^{29}Si MAS NMR spectroscopy. In Fig. 3 the silicon spectra of the different materials before and after etching are depicted. Interestingly, depending on the concentration of the pre-hydrolized TEOS solution different siliceous species could be formed. For low amounts (10 : 1 and 5 : 1 samples) the presence of Q0, Q1 and Q2 sites suggests the formation of monomeric, dimer and oligomeric units. At higher contents (2 : 1 and 1 : 1 samples) the condensation reaction is promoted, and Q3 and Q4 signals, ascribed to a pure SiO_2 structure, further appear. After treatment with NaOH, the silica was completely removed and only a small fraction of Q0 and Q1 sites was left. These siliceous rests can be associated with silicate phases.[34] This finding is corroborated also by XRD measurements of the materials calcined at higher temperature (700–900 °C, Fig. 2c).

The atomic ratios in the materials could be determined by XPS, providing also information on chemical environment and

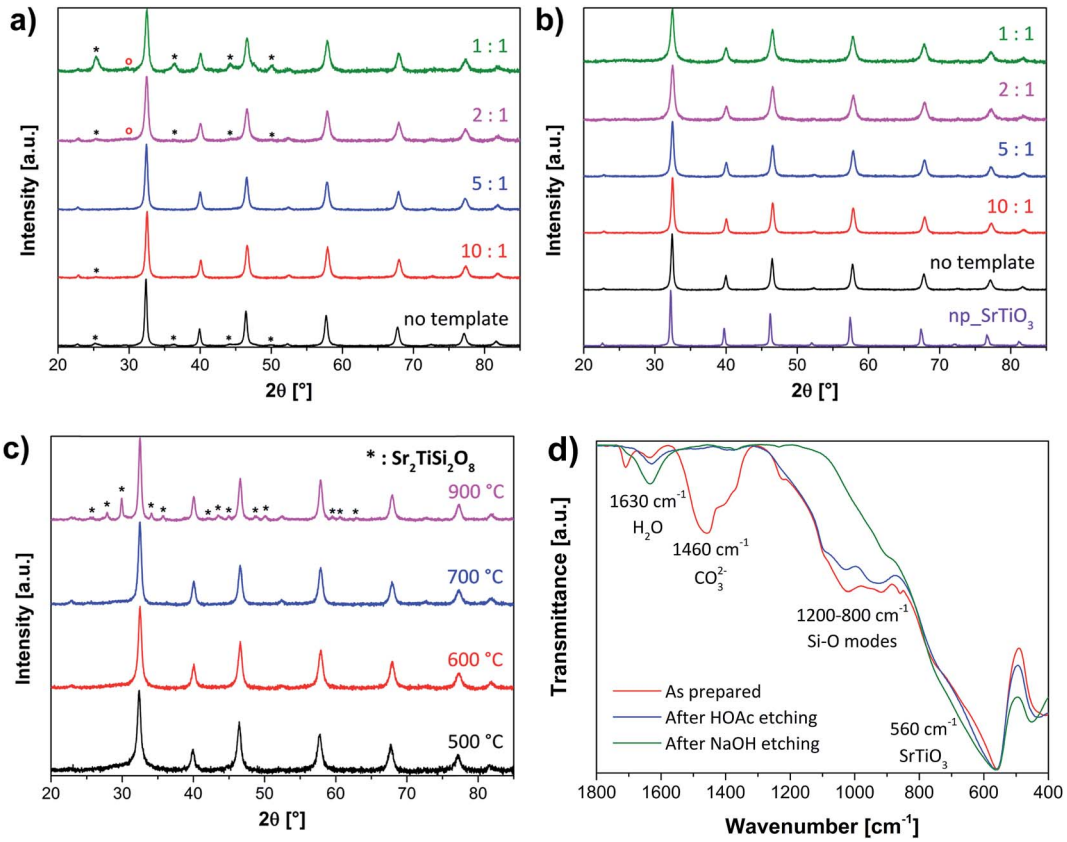

Fig. 2 (a–c) X-ray diffractograms of different $SrTiO_3$ samples: (a) as-prepared systems with different $SrTiO_3$: SiO_2 molar ratios calcined at 600 °C. The asterisks identify $SrCO_3$ impurities whereas the siliceous phase is marked with the red circles; (b) final mesoporous materials obtained with different $SrTiO_3$: SiO_2 molar ratios calcined at 600 °C along with commercially available nanoparticulate $SrTiO_3$ (np_$SrTiO_3$); (c) as-prepared sample 2 : 1 (molar ratio $SrTiO_3$: SiO_2) at different calcination temperatures. The asterisks indicate $Sr_2TiSi_2O_8$ phase. (d) Infrared spectra of the 2 : 1 sample at different synthesis steps, taken as representative example for all the materials.

Table 1 Specific surface area (S_{BET}) and pore volume (V_P) determined by nitrogen physisorption; crystallite size (Φ) obtained by XRD; bang-gap energy (E_{BG}) calculated from the Kubelka–Munk plots of the materials' UV spectra; apparent (k_{app}) and normalized (K_{norm}) reaction rate constants for the degradation of MB; atomic composition of the as-prepared samples along with the residual amount of silicon after etching procedure (Si_e)

Sample	S_{BET} [$m^2\ g^{-1}$]	V_P [$cm^3\ g^{-1}$]	Φ [nm]	E_{BG} [eV]	k_{app} [min^{-1}]	K_{norm} [$gm^{-2}\ min^{-1}$]	C [% at]	O [% at]	Ti [% at]	Sr [% at]	Si [% at]	Si_e [% at]
No template	60	0.22	31	3.20	2.1×10^{-3}	3.5×10^{-5}	15.5	55.3	14.9	14.2	—	—
10 : 1	79	0.23	26	3.24	3.0×10^{-3}	3.8×10^{-5}	9.8	58.4	15	13.8	3.2	1.1
5 : 1	114	0.29	23	3.24	4.4×10^{-3}	3.9×10^{-5}	15.2	54.8	13.8	12.1	4.1	2.2
2 : 1	216	0.36	17	3.27	7.2×10^{-3}	3.3×10^{-5}	8.2	61.8	13.6	9.5	6.7	1.7
1 : 1	239	0.39	15	3.27	1.1×10^{-2}	4.6×10^{-5}	12.3	59.3	9.9	7.2	11.2	3
np_$SrTiO_3$	38	—	48	3.31	2.0×10^{-4}	5.3×10^{-6}	—	—	—	—	—	—

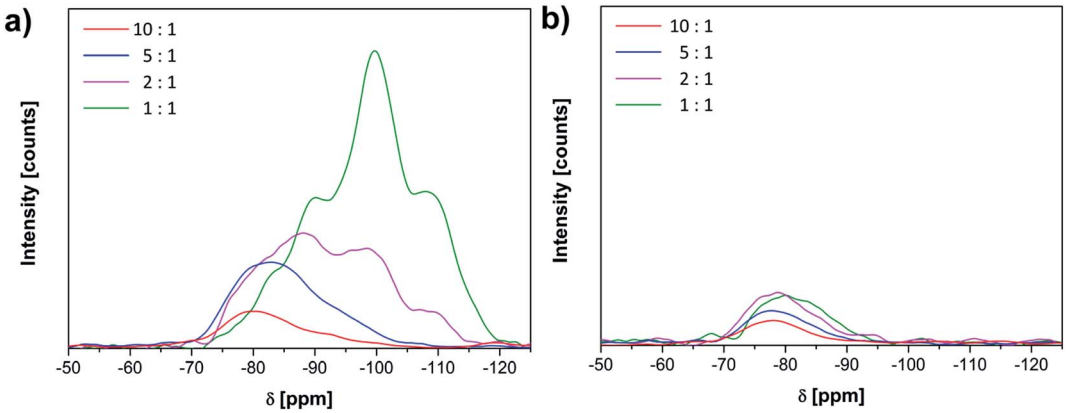

Fig. 3 ^{29}Si CP-MAS NMR spectra of the $SrTiO_3$ samples before (a) and after NaOH etching (b). Q0 site at *ca.* −78 ppm; Q1 at −85 ppm; Q2 at *ca.* −90 ppm; Q3 at −100 ppm and Q4 at −110 ppm.

oxidation state of the species of interest. First, a survey spectrum was acquired for all samples. In Fig. 4, the spectrum of sample 1 : 1 before and after etching is plotted, to representative show that all element of interest (Si, Sr, Ti, O, C) can be identified. The retrieved binding energies are in agreement with the expected oxidation states, *i.e.* Si(IV), Sr(II) and Ti(IV). Afterwards, selected regions were acquired with higher resolution for the quantitative determination of the atomic percentages. In this way, it could be shown that the stoichiometric ratios $SrTiO_3$: SiO_2 of the as prepared materials correspond well to the nominal values (Table 1). However, slight deviations can be found especially for the Ti/Sr ratio, which is higher in the 1 : 1 and 2 : 1 materials than in the others. This result can be ascribed to a surface effect determined by silica enrichment, which affects the distribution of the metal species.[35]

The relatively high carbon amount originates from both carbonates and surface contaminations contributions. Moreover, the efficacy of the etching procedure is proven by the very little residual atomic amount of silicon (Si_e), in very good agreement with the NMR results.

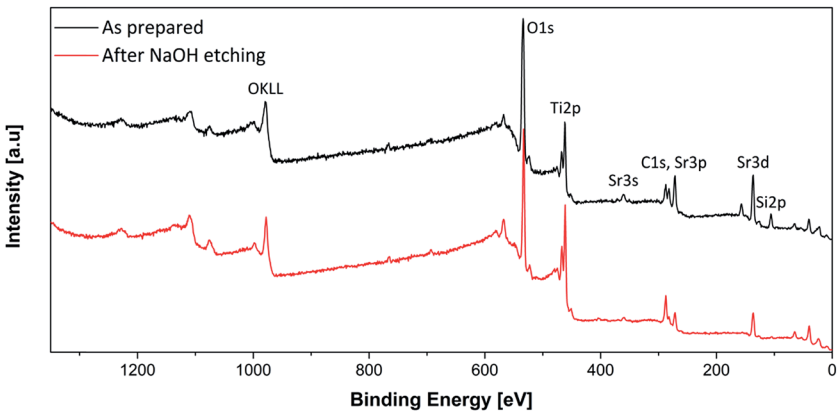

Fig. 4 Survey spectrum of the sample 1 : 1 before and after NaOH etching.

Nitrogen physisorption was used to assess the porosity of the materials. In Fig. 5, the physisorption analyses of the nanoporous $SrTiO_3$ obtained by different amounts of silica template are displayed. All curves are characterized by type IV(a) isotherms[36] with broad hysteresis. The steep increase close to the saturation pressure can be assigned to interparticle porosity. As expected, specific surface area and pore volume constantly increase upon silica loading (Table 1). The effect of the hard template on the textural properties is more evident for the size of the pores (Fig. 5b). Very broad distributions are formed for low silica content and "no template" $SrTiO_3$. Here, the siliceous phase poorly participates to the pore generation, most probably because the oligomeric structure and the low concentration are not sufficient to build a three-dimensional network. For quantities larger than 20% more condensed silica species are built (Fig. 3a), which interpenetrate the $SrTiO_3$ matrix and form additional porosity. This templating action is clearly visible by the progressive narrowing of the pore size distribution towards 6 nm.

Only slight differences can be distinguished between the 2 : 1 and 1 : 1 samples. In the light of NMR results (Fig. 3a), one would expect much larger porosity and pore size for the 1 : 1 system. The larger amount of Q3 and Q4 sites observed by ^{29}Si MAS NMR apparently does not actively participate to the templating and eventually belong to SiO_2 domains which phase-separate.

Additional information on material and pore morphology could be obtained by electron microscopy analyses. All porous $SrTiO_3$ forms grains of several micrometers with surfaces studded with pores of *ca.* 20 nm (Fig. 6b). For the samples prepared with high SiO_2 content, TEM analysis shows disordered distribution of interconnected pores of approx. 10 nm (Fig. 6c) and crystalline pore walls in very good agreement with nitrogen physisorption and XRD.

Diffuse reflectance UV spectroscopy (DR-UV) was used to determine the light absorption properties of the investigated materials. The band gap energy (E_{BG}) was calculated from the linear fit of the modified Kubelka-Munk function $(F(R)h\nu)^{0.5}$ *vs.* $h\nu$ (Tauc plot, Fig. 7a).[37] The values of the linearization fitting are given in Table S1.† All the systems have similar band gap of

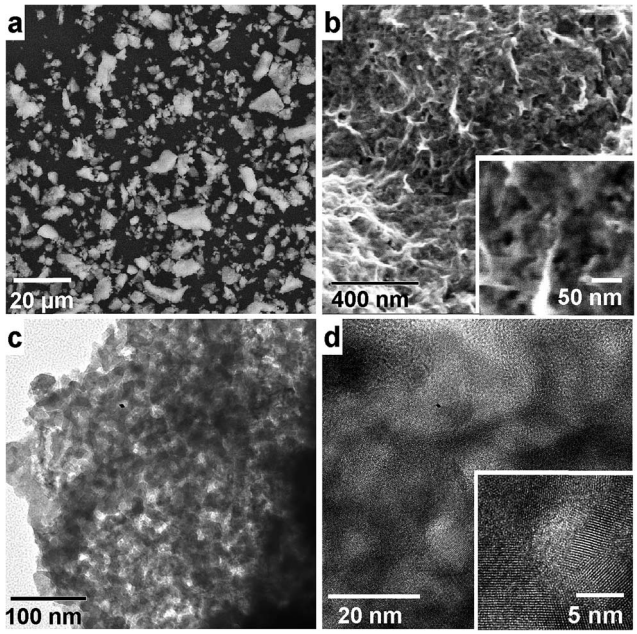

Fig. 6 SEM (a, b), TEM overview (c) and HRTEM (d) micrographs of mesoporous 2 : 1 sample chosen as representative system. The insets are enlarged viewings of the corresponding SEM and HRTEM micrographs.

ca. 3.25 eV, in line with literature results.[13,38] Slight variations are evident, which can be ascribed to both diverse nanostructure and preparation method. The band gap increase in the bulk materials (Table 1) is explained both by the higher porosity,[39,40] and by the decrease of crystallite size. Such structure variation triggers quantum size effects, which determine the band gap widening.[41,42] As a consequence, a blueshift of the UV spectra is clearly visible, especially for the 1 : 1 sample. These results are in very good agreement with values published by Li *et al.*[13] on similar mesoporous $SrTiO_3$ nanoparticels. The material synthesis conditions have also significant impact on the band gap of metal oxides,[37] which might explain the larger value for commercial $SrTiO_3$ nanoparticles (np_$SrTiO_3$). Moreover, the different absorption behavior of the templated systems

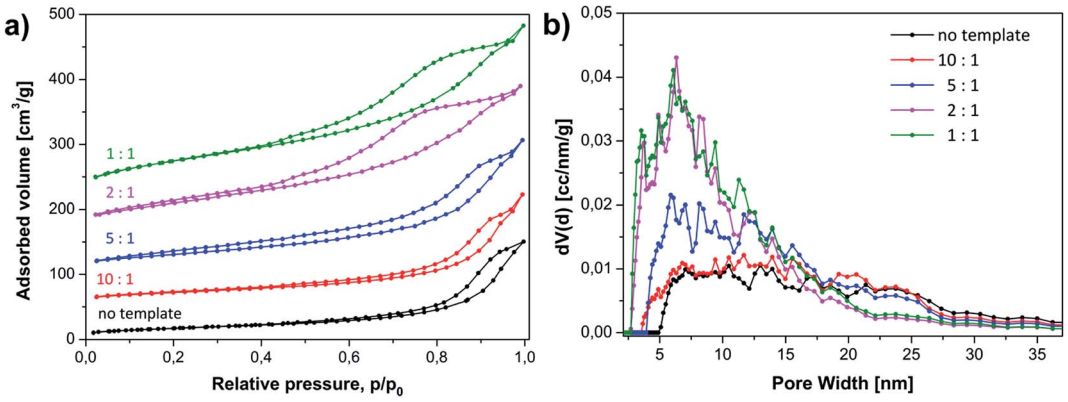

Fig. 5 N_2 physisorption isotherms (a) and pore size distribution (b) of the different mesoporous $SrTiO_3$ materials. Each isotherm is shifted upward by 50 $cm^3\ g^{-1}$ for clarity except for the data referring to pure $SrTiO_3$.

with respect to pure $SrTiO_3$ can be justified by alkalinization of the material surface occurring during the NaOH treatment.[38]

As mentioned before, $SrTiO_3$ has been reported to exhibit interesting photocatalytic properties.[12,13,27] The catalytic activity of our systems was exemplary studied by the photodegradation of methylene blue (MB) dye for potential waste-water treatment applications (Fig. 7b, S2b†). The effect of the silica template on the degradation of the MB can be observed in Fig. 7c. As reference, commercially available nanoparticulate $SrTiO_3$ was used. The SiO_2-free sample, prepared by the standard chelate complex method, resulted to be 15% more active than np_$SrTiO_3$. The extent of dye degradation progressively increased with the increasing template content until a maximum of 75% for the nanoporous 1 : 1 sample. In addition, a basic analysis of the kinetic was performed to obtain better insight into the MB photodegradation. For each catalyst, the plot of $\ln(C/C_0)$ *vs.* reaction time yielded almost a straight line (Fig. S3†), the slope of which indicates the apparent reaction constant k_{app}. This suggests that the photocatalytic decomposition of MB by all $SrTiO_3$ samples follows an apparent kinetics law of first order, as can be also deduced by Fig. 7c. In particular, 1 : 1 nanoporous aggregates display an apparent degradation rate constant of 1.1×10^{-2} min^{-1}, which is much higher compared to the values obtained for nanoparticulated and no templated $SrTiO_3$ (Table 1). Moreover, the normalized rate constant K_{norm} defined as $K_{norm} = k_{app}/S_{BET}$ for the degradation of MB revealed that the enhanced catalytic properties of the porous materials can be clearly related with their larger surface area, as expected.

In general, the photocatalytic dye degradation on transition metal oxides depends on two important processes namely, the absorption of the light followed by the separation of the e^-/h^+ pairs and the adsorption of organic molecules on the catalyst surface.[43] These phenomena depend respectively by the microstructure and the porosity of the materials, and their analysis can help to better understand the photocatalytic behavior of the materials. Dye adsorption over the porous $SrTiO_3$ samples after 1 h dark-stirring of the stock solution has shown to constantly increase with the surface area of the materials up to approx. 6 times with respect to the template-free material (Fig. 7d). Interestingly, it can be observed that the adsorption for the 10 : 1 sample is *ca.* 150% more than for the not templated one, even though both systems have similar surface area and porosity. With respect to pure $SrTiO_3$, the 10 : 1 sample underwent NaOH treatment, which have possibly alkalized the surface.[38] Hence, this process mighty have not only modified the absorption of the light (Fig. 7a) but also created stronger adsorption sites, thus explaining the higher dye adsorption and conversion. Moreover, although the materials obtained with larger concentration of silica have comparable dye adsorption capacities, the degradation potential of the 1 : 1 sample is significantly larger. This effect depends thus exclusively by light

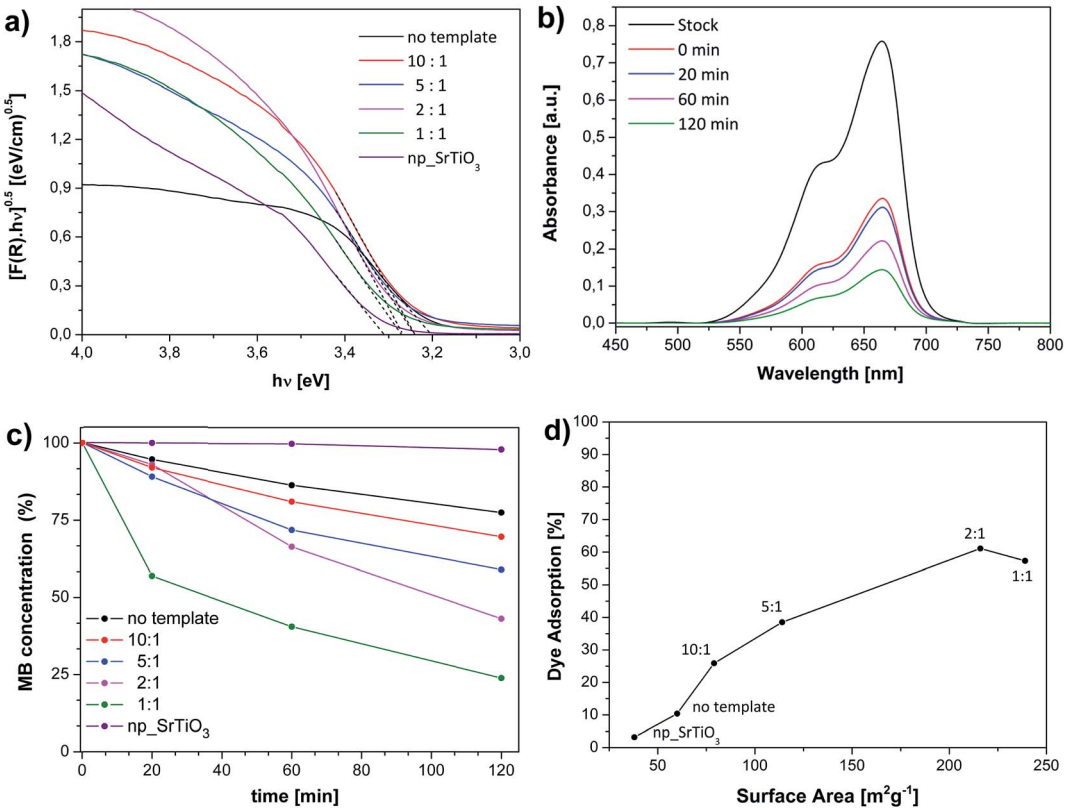

Fig. 7 UV-Vis spectra of the tested materials (Tauc plot, a) and of methylene blue over the mesoporous 2 : 1 sample after different irradiation times (b). Extent of dye degradation achieved upon 2 h irradiation (c) and dye adsorption after 1 h dark-stirring of the stock solution (d) for the tested $SrTiO_3$ samples.

absorption capacity and is most probably determined by the prominent quantum size effects (blueshift of the material UV-spectrum), which enable good separation of the charge carriers.[11,43]

Hence, the mutual variation of porous and microstructural properties clearly explains the superior catalytic properties of the samples prepared with larger amount of silica with respect to the non-porous ones. Moreover we could observe that the activity of our systems is nicely in agreement with similar dye photodegradation studies on mesoporous $SrTiO_3$ nanoparticles.[11]

Conclusions

Mesoporous bulk $SrTiO_3$ was synthesized by a novel route, using the cooperative assembly of metal chelate complexes and alkoxysilanes. The high affinity and intimate mixing between the two precursors fostered the formation, *via* poly-condensation of interpentrating organic–inorganic polymers. Pure crystalline mesoporous $SrTiO_3$ with highly interconnected pores resulted after calcination of the organic phase and removal of the silica phase *via* NaOH etching.

Variation of porosity and crystallinity were obtained using different SiO_2-to-$SrTiO_3$ molar ratios (0.1–1). The templating action of the silica and its effect on the structure and morphology of the final systems were addressed by a multi technique approach.

In particular, ^{29}Si-MAS NMR analyses pointed out that at low concentrations of template only monomeric and oligomeric domains of silica could be formed. On the contrary, significant condensation of the siloxane groups and formation of dense domains occurred for concentrations larger than 20%. All the siliceous species were successfully removed *via* etching with exception of a small fraction of silicates.

The porous properties of the final perovskite reproduce very well the structural evolution of the silica in the nanocomposite materials. Hence, only at high SiO_2 concentrations the condensed silica species acted as real template leading to the formation of large surface areas with narrower pore sizes. In addition, constant decrease of the $SrTiO_3$ crystallite size upon increasing SiO_2 content was observed owing to the hampered mass transport of the perovskite phase.

Finally, the activity of the mesoporous perovskites was exemplarily demonstrated by photocatalytic degradation tests of methylene blue. The dye conversion progressively increased with the content of silica template up to 7 times than for the corresponding non-porous system, as a result of the combined increase of porosity and decrease of crystallite size.

The presented cooperative assembly synthesis approach represents therefore an easy and reproducible approach to obtain photoactive mesoporous bulk crystalline $SrTiO_3$ materials with large porosity and interconnected mesopores. Moreover, the high thermal stability of the porous structure and the flexible tuning of the composition offered by the metal complexes allow the implementation for other pure and doped perovskite oxide systems for energy-relevant (*e.g.* redox) catalysis applications.

Acknowledgements

Uta Sazama, Sandra König and Isabelle Nevoigt of the University of Hamburg are gratefully acknowledged for the help with the thermal, physisorption and X-ray diffraction analyses.

References

1 J. H. Haeni, P. Irvin, W. Chang, R. Uecker, P. Reiche, Y. L. Li, S. Choudhury, W. Tian, M. E. Hawley, B. Craigo, A. K. Tagantsev, X. Q. Pan, S. K. Streiffer, L. Q. Chen, S. W. Kirchoefer, J. Levy and D. G. Schlom, *Nature*, 2004, **430**, 758–761.
2 K. van Benthem, C. Elsässer and R. H. French, *J. Appl. Phys.*, 2001, **90**, 6156.
3 R. A. De Souza, *Adv. Funct. Mater.*, 2015, **25**, 62326–66342.
4 P. Lupetin, G. Gregori and J. Maier, *Angew. Chem., Int. Ed.*, 2010, **49**, 10123–10126.
5 H. Ohta, S. Kim, Y. Mune, T. Mizoguchi, K. Nomura, S. Ohta, T. Nomura, Y. Nakanishi, Y. Ikuhara, M. Hirano, H. Hosono and K. Koumoto, *Nat. Mater.*, 2007, **6**, 129–134.
6 A. V. Kovalevsky, A. A. Yaremchenko, S. Populoh, A. Weidenkaff and J. R. Frade, *J. Phys. Chem. C*, 2014, **118**, 4596–4606.
7 F. Messerschmitt, M. Kubicek, S. Schweiger and J. L. M. Rupp, *Adv. Funct. Mater.*, 2014, **24**, 7448–7460.
8 T. Sakuma, S. Yamamichi, S. Matsubara, H. Yamaguchi and Y. Miyasaka, *Appl. Phys. Lett.*, 1990, **57**, 2431.
9 P. Reunchan, S. Ouyang, N. Umezawa, H. Xu, Y. Zhang and J. Ye, *J. Mater. Chem. A*, 2013, **1**, 4221.
10 X. Zhou, N. Yan, K. T. Chuang and J. Luo, *RSC Adv.*, 2014, **4**, 118–131.
11 H. Zhan, Z. G. Chen, J. Zhuang, X. Yang, Q. Wu, X. Jiang, C. Liang, M. Wu and J. Zou, *J. Phys. Chem. C*, 2015, **119**, 3530–3537.
12 S. Ouyang, P. Li, H. Xu, H. Tong, L. Liu and J. Ye, *ACS Appl. Mater. Interfaces*, 2014, **6**, 22726–22732.
13 H. Liu, X. Chen, S. Yan, Z. Li and Z. Zou, *Eur. J. Inorg. Chem.*, 2014, **23**, 3731–3735.
14 J. H. Pan, C. Shen, I. Ivanova, N. Zhou, X. Wang, W. C. Tan, Q. H. Xu, D. W. Bahnemann and Q. Wang, *ACS Appl. Mater. Interfaces*, 2015, **7**, 14859–14869.
15 G. Xu, S. Deng, Y. Zhang, X. Wei, X. Yang, Y. Liu, G. Shen and G. Han, *CrystEngComm*, 2014, **16**, 2025.
16 J.-Q. Zheng, Y.-J. Zhu, J.-S. Xu, B.-Q. Lu, C. Qi, F. Chen and J. Wu, *Mater. Lett.*, 2013, **100**, 62–65.
17 M. Kakihana, T. Okubo, M. Arima, Y. Nakamura, M. Yashima and M. Yoshimura, *J. Sol-Gel Sci. Technol.*, 1998, **12**, 95–109.
18 M. Kakihana and M. Yoshimura, *Bull. Chem. Soc. Jpn.*, 1999, **72**, 1427–1443.
19 S. Diodati, L. Nodari, M. M. Natile, A. Caneschi, C. de J. Fernandez, C. Hoffmann, S. Kaskel, A. Lieb, V. Di Noto, S. Mascotto, R. Saini and S. Gross, *Eur. J. Inorg. Chem.*, 2014, **5**, 875–887.
20 C. Sanchez, C. Boissière, D. Grosso, C. Laberty and L. Nicole, *Chem. Mater.*, 2008, **20**, 682–737.

21 B. L. Cushing, V. L. Kolesnichenko and C. J. O'Connor, *Chem. Rev.*, 2004, **104**, 3893–3946.
22 D. Grosso, C. Boissière, B. Smarsly, T. Brezesinski, N. Pinna, P. A. Albouy, H. Amenitsch, M. Antonietti and C. Sanchez, *Nat. Mater.*, 2004, **3**, 787–792.
23 T. Puangpetch, T. Sreethawong, S. Yoshikawa and S. Chavadej, *J. Mol. Catal. A: Chem.*, 2008, **287**, 70–79.
24 J. Lee, J. Kim, Y. Lee, S. Yoon, S. M. Oh and T. Hyeon, *Chem. Mater.*, 2004, **16**, 3323–3330.
25 R. Liu, Y. Shi, Y. Wan, Y. Meng, F. Zhang, D. Gu, Z. Chen, B. Tu and D. Zhao, *J. Am. Chem. Soc.*, 2006, **128**, 11652–11662.
26 O. Sel, S. Sallard, T. Brezesinski, J. Rathouský, D. R. Dunphy, A. Collord and B. M. Smarsly, *Adv. Funct. Mater.*, 2007, **17**, 3241–3250.
27 X. Fan, Y. Wang, X. Chen, L. Gao, W. Luo, Y. Yuan, Z. Li, T. Yu, J. Zhu and Z. Zou, *Chem. Mater.*, 2010, **22**, 1276–1278.
28 S. Brunauer, P. H. Emmett and E. Teller, *J. Am. Chem. Soc.*, 1938, **60**, 309–319.
29 P. I. Ravikovitch and A. V. Neimark, *J. Phys. Chem. B*, 2001, **105**, 6817–6823.
30 D. Briggs and M. P. Seah, *Practical surface analysis: by auger and X-ray photo-electron spectroscopy*, Wiley, 1983.
31 J. F. Moulder, W. F. Stickle, P. E. Sobol and K. D. Bomben, *Handbook of X-ray Photoelectron Spectroscopy*, Eden Praire, 1992.
32 D. A. Shirley, *Phys. Rev. B: Condens. Matter Mater. Phys.*, 1972, **5**, 4709–4714.
33 T. M. Breault and B. M. Bartlett, *J. Phys. Chem. C*, 2012, **116**, 5986–5994.
34 M. Andrianainarivelo, R. Corriu, D. Leclercq, P. H. Mutin and A. Vioux, *J. Mater. Chem.*, 1996, **6**, 1665.
35 D. C. M. Dutoit, M. Schneider and A. Baiker, *Chem. Eng.*, 1996, **439**, 433–439.
36 M. Thommes, K. Kaneko, A. V. Neimark, J. P. Olivier, F. Rodriguez-Reinoso, J. Rouquerol and K. S. W. Sing, *Pure Appl. Chem.*, 2015, 1051–1069.
37 R. López and R. Gómez, *J. Sol-Gel Sci. Technol.*, 2012, **61**, 1–7.
38 S. Ouyang, H. Tong, N. Umezawa, J. Cao, P. Li, Y. Bi, Y. Zhang and J. Ye, *J. Am. Chem. Soc.*, 2012, **134**, 1974–1977.
39 K. Wang, Y. Liu and Q. S. Yang, *Ultrasonics*, 2015, **61**, 25–32.
40 Y. Liu, J. Y. Su, Y. L. Xu and X. C. Zhang, *Ultrasonics*, 2009, **49**, 276–280.
41 E. Monaico, V. V. Ursaki, I. M. Tiginyanu, Z. Dashevsky, V. Kasiyan and R. W. Boyd, *J. Appl. Phys.*, 2006, **100**, 1–6.
42 N. Satoh, T. Nakashima, K. Kamikura and K. Yamamoto, *Nat. Nanotechnol.*, 2008, **3**, 106–111.
43 X. Chen, S. Shen, L. Guo and S. S. Mao, *Chem. Rev.*, 2010, **110**, 6503–6570.